

# Optical, electrical, and solar energy-conversion properties of gallium arsenide nanowire-array photoanodes†

Cite this: *Energy Environ. Sci.*, 2013, **6**, 1879

Shu Hu,<sup>ad</sup> Chun-Yung Chi,<sup>‡b</sup> Katherine T. Fountaine,<sup>‡ad</sup> Maoqing Yao,<sup>‡b</sup> Harry A. Atwater,<sup>‡\*cd</sup> P. Daniel Dapkus,<sup>‡\*b</sup> Nathan S. Lewis<sup>‡\*ad</sup> and Chongwu Zhou<sup>‡b</sup>

Periodic arrays of n-GaAs nanowires have been grown by selective-area metal–organic chemical-vapor deposition on Si and GaAs substrates. The optical absorption characteristics of the nanowire-arrays were investigated experimentally and theoretically, and the photoelectrochemical energy-conversion properties of GaAs nanowire arrays were evaluated in contact with one-electron, reversible, redox species in non-aqueous solvents. The radial semiconductor/liquid junction in the nanowires produced near-unity external carrier-collection efficiencies for nanowire-array photoanodes in contact with non-aqueous electrolytes. These anodes exhibited overall inherent photoelectrode energy-conversion efficiencies of  $\sim 8.1\%$  under  $100 \text{ mW cm}^{-2}$  simulated Air Mass 1.5 illumination, with open-circuit photovoltages of  $590 \pm 15 \text{ mV}$  and short-circuit current densities of  $24.6 \pm 2.0 \text{ mA cm}^{-2}$ . The high optical absorption, and minimal reflection, at both normal and off-normal incidence of the GaAs nanowire arrays that occupy  $<5\%$  of the fractional area of the electrode can be attributed to efficient incoupling into radial nanowire guided and leaky waveguide modes.

Received 23rd January 2013

Accepted 14th March 2013

DOI: 10.1039/c3ee40243f

[www.rsc.org/ees](http://www.rsc.org/ees)

## Broader context

Due to the voltage requirements to produce fuels from sunlight, water, and  $\text{CO}_2$  as the inputs, two light-absorbing materials, with band gaps of 1.7 eV and 1.1 eV, respectively, are attractive as the foundation for high-efficiency artificial photosynthesis. The integration of materials with 1.7 and 1.1 eV band gaps is, however, very challenging. Accordingly, a nanowire-growth strategy has been developed to integrate single crystal III–V nanowires (e.g. GaAs) with highly mismatched Si substrates. In this work, GaAs nanowire arrays grown on Si were studied using a non-destructive contact method involving non-aqueous photoelectrochemistry. The approach has allowed us to understand the interplay of nanowire growth with the optical absorption and electrical properties of such systems, and will aid in the design and optimization of nanowire-based systems for solar energy-conversion applications.

Photoelectrolysis of water for the production of renewable  $\text{H}_2$  from sunlight faces a constraint in that a potential difference of 1.23 V is required thermodynamically to sustain the water-splitting reaction under standard conditions. In an integrated photoelectrochemical system for water splitting, the operating voltage produced by the light absorber should exceed the sum of the thermodynamic minimum required potential difference,

the resistance losses of electrolytes, and any overpotentials that are required to drive water splitting at a given current density in the device structure of interest. When this requirement is met, the solar-to-hydrogen (STH) efficiency is limited solely by the photocurrent density generated from the light absorber.

By sequentially stacking light-absorbing materials with different band gaps to utilize various wavelengths of light in the solar spectrum, a dual-junction tandem structure can provide a sufficient photovoltage as well as high current densities to drive the water-splitting reaction. Assuming that the combined overpotentials for the hydrogen-evolution and oxygen-evolution reactions are 450 mV at a current density of  $25 \text{ mA cm}^{-2}$ , and assuming that the resistance to ionic transport is 10 ohm, a theoretical STH efficiency of 27.0% is possible for a 1.7 eV/1.1 eV tandem band-gap pair under Air Mass (AM) 1.5G 1-Sun illumination.<sup>1</sup> Under these conditions, epitaxial, lattice-matched, dual-junction light absorbers formed from a 1.85 eV/1.42 eV InGaP/GaAs combination would provide a theoretical STH efficiency of

<sup>a</sup>Division of Chemistry and Chemical Engineering, 210 Noyes Laboratory, California Institute of Technology, Pasadena, CA, 91125, USA. E-mail: [nslewis@caltech.edu](mailto:nslewis@caltech.edu)

<sup>b</sup>Ming Hsieh Department of Electrical Engineering, University of Southern California, Los Angeles, CA, USA

<sup>c</sup>Department of Applied Physics and Materials Science, California Institute of Technology, Pasadena, CA, 91125, USA

<sup>d</sup>Joint Center for Artificial Photosynthesis, California Institute of Technology, 1200 E. California Blvd., Pasadena, CA, 91125, USA

† Electronic supplementary information (ESI) available. See DOI: 10.1039/c3ee40243f

‡ These authors made equal contributions.

16.9%. Light absorbers that consist of more than two materials will provide more photovoltage and less photocurrent density, in general, and thus are not optimal for water splitting.

For a dual-junction solar cell, the detailed-balance calculation that considers no angular restriction in photoemission sets an optimal efficiency limit of 43.6% at 1-Sun for a band gap combination of 1.7 eV/1.1 eV,<sup>2</sup> whereas the reported record efficiency for epitaxial InGaP/GaAs solar cells is 30.9% at 1-Sun,<sup>3</sup> still far from the theoretical limit. Planar, dual-junction, semiconductor light absorbers are typically constrained by the requirement that the two semiconductor materials must be essentially lattice-matched to realize high-quality growth of the materials. Structures with 1.7 eV/1.1 eV band-gap combinations could be produced by the growth of lattice-mismatched thin films, *e.g.* III–V ternary compounds on silicon–germanium (SiGe), but large lattice-mismatches and polar–nonpolar interfaces between III–V materials and Si(Ge) can lead to deleterious threading dislocations and a high density of interfacial defects, thus adversely affecting the energy-conversion performance of such devices.<sup>4,5</sup> Because the lattice-matching criterion restricts the accessible band-gap combinations that can be produced experimentally, design schemes for integration of highly mismatched light absorbers having 1.7 eV/1.1 eV band gaps are very attractive for both solar water-splitting and solar photovoltaic applications.

The lattice-mismatched growth of III–V nanowire-arrays on silicon (Si,  $E_g = 1.12$  eV) is one strategy for fabrication of high quality, dissimilar, and current-matched light absorbers. The small cross-sectional area of nanowires (NWs) allows for elastic relaxation of the strain induced by the lattice mismatch between the nanowires and the substrate.<sup>6,7</sup> Furthermore, a 1.7 eV/1.1 eV band gap tandem structure would produce optimal energy-conversion efficiencies that are comparable to those of commercial triple-junction cells obtained by lattice-matched growth of inorganic III–V semiconductors.<sup>8–11</sup> The use of Si substrates, and the low filling-fraction of NW arrays, would significantly reduce the materials cost by allowing the replacement of the expensive planar III–V or Ge substrates.

In this work, the optical, electrical and photoelectrochemical energy-conversion properties of periodic arrays of GaAs NWs grown on Si and GaAs have been systematically investigated *via* experiment and theory. Although the performance of Si or GaAs-based nanowire photovoltaics has been described previously,<sup>12,13</sup> the GaAs ( $E_g = 1.42$  eV) used herein serves as a model system to demonstrate the quality of NW-array light absorbers enabled by the III–V NW-on-Si strategy. Several compounds that satisfy the 1.7 eV band gap requirement can be obtained in the composition space afforded by ternary and quaternary III–V semiconductors.<sup>14–16</sup> Subsequently, this NW-on-Si strategy can therefore be applied to ternary  $\text{In}_{0.65}\text{Ga}_{0.35}\text{P}$ ,  $\text{GaAs}_{0.78}\text{P}_{0.22}$ ,  $\text{Al}_{0.20}\text{GaAs}_{0.80}$  NWs and/or to quaternary systems<sup>17–19</sup> that have a 1.7 eV direct band gap.

GaAs NWs can be synthesized by selective-area growth (SAG) or by vapor–liquid–solid (VLS) growth *via* metal–organic chemical–vapor deposition (MOCVD). SAG has been used to synthesize GaAs,<sup>20</sup> GaP, InP<sup>21</sup> and InAs<sup>22</sup> NWs. Using a nano-patterned mask, III–V nanowires with hexagonal cross-sections can be grown on either (111)A- or (111)B-oriented III–V substrates *via* vapor-solid deposition. High-yield vertically oriented GaAs<sup>23</sup> and InAs<sup>24</sup>

nanowires have been produced on non-polar Si substrates, demonstrating the growth of III–V NWs on lattice-mismatched, inexpensive substrates. III–V NWs can also be fabricated by a vapor–liquid–solid (VLS) growth method, in which the precursors in their vapor phase are dissolved into the liquid phase of metal catalysts (*e.g.* Au or Ga) that then initiate the growth of NWs. The VLS-catalyzed growth of III–V NWs on Si substrates has also been demonstrated,<sup>25,26</sup> but with lower fidelity than SAG growth. Although high crystal quality can be obtained from VLS-grown III–V NWs, the catalyst material can be unintentionally incorporated into the NWs during growth, possibly creating deep-level traps that can degrade the electrical performance of the resulting devices. Ga-assisted VLS has been proposed to address this issue, but the solubility of ionizable dopants in liquid VLS catalysts is often large enough to prevent facile production of abrupt doping and composition transitions. We have therefore used the SAG method to grow III–V NW/Si substrate structures.

Fig. 1a illustrates the gas flow and temperature profiles as a function of time for growth of n-GaAs NWs on an  $n^+$ -Si substrate. The Si (111) substrate (phosphorus doped, doping concentration  $0.8\text{--}1.3 \times 10^{18} \text{ cm}^{-3}$ , to eliminate Si photo-activity) was patterned with a silicon nitride ( $\text{SiN}_x$ ) mask by electron-beam lithography. Initially, the patterned Si substrate was annealed in  $\text{H}_2(\text{g})$  at 965 °C for 5 min to remove residual silicon oxide in the openings of the mask. The Si substrate was then annealed in  $\text{AsH}_3$  at 440 °C for 2 min to create an As-passivated Si surface that resembled a GaAs (111)B surface. The formation of the As-terminated surface was crucial to attaining high-fidelity growth of the GaAs NWs. A low-temperature nucleation step at 440 °C for 8 min in the presence of trimethylgallium (TMGa) and arsine ( $\text{As}_2\text{H}_6$ ) was then followed by a high-temperature step for nanowire growth at 790 °C for 30–60 min, with disilane ( $\text{Si}_2\text{H}_6$ ) as the n-dopant source. Fig. 1b illustrates the gas flow and temperature profiles as a function of time for the growth of GaAs NWs on an  $n^+$ -GaAs (111)B substrate (Si doped, doping concentration  $3 \times 10^{18} \text{ cm}^{-3}$ ). High-temperature annealing and low-temperature nucleation steps were not necessary in this process flow to produce GaAs NWs.

The length of GaAs NWs was determined by the duration of the growth, whereas the diameter and pitch of the nanowires in the array were defined by electron-beam lithography. Fig. 1c displays a typical SEM image of arrays of GaAs NWs that were grown on a Si substrate (also however being representative of typical arrays of GaAs NWs that were grown on a GaAs substrate). The measured diameter of the GaAs NWs on Si or GaAs substrates was  $\sim 135$  nm, and the pitch was 600 nm. A 600 nm pitch was chosen to minimize the bunching of wires that occurred during processing and to accommodate the limitations on wire diameter that were imposed by the lattice-mismatched growth. The GaAs NWs on Si substrates were 2.5  $\mu\text{m}$  long from a 30 min growth, and the GaAs NWs on GaAs substrates were 3  $\mu\text{m}$  long from a 1 h growth. Longer growth times did not significantly improve the optical absorption of the resulting NW arrays. High-resolution transmission-electron microscopy (Fig. 1d) indicated that the GaAs NWs had a zinc blende crystal structure, {110}-type sidewall facets, and a high density of twin defects along the (111)B growth direction.

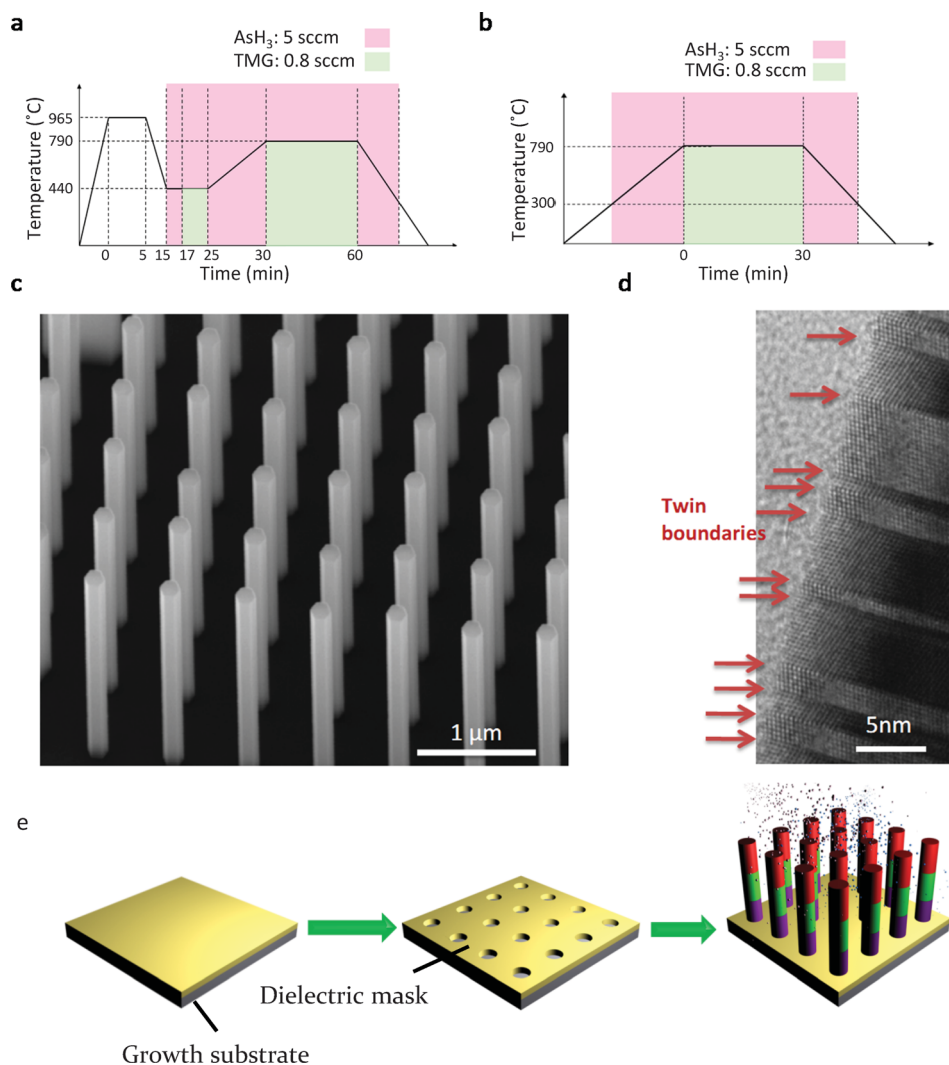


**Fig. 1** Growth schematics and structural characterization of n-GaAs NWs after MOCVD at 790 °C. (a and b) Schematic illustrations of the gas flow and temperature sequence for growth of GaAs NWs on Si and on GaAs, respectively. (c) 30° from plan-view scanning electron microscope image of arrays of GaAs NWs grown on Si substrates. (d) Transmission electron microscope image of a single GaAs NW. The incident electron beam was normal to the (110) facet. The red arrows indicate twin boundaries along the (111)B growth direction. (e) Process schematics of selective-area MOCVD growth.

To measure the optical properties, free-standing GaAs NW arrays were embedded in a thin film of polydimethylsiloxane (PDMS) and exfoliated from the substrate (see ESI†). Fig. 2a compares the optical absorption at normal incidence of a GaAs NW-array embedded in PDMS, an array embedded in PDMS on a silver (Ag) back reflector, and the as-grown array on a GaAs substrate. The absorption of the array that also had a back reflector exhibited broadband enhancement relative to the absorption of the array embedded in PDMS, because the back reflector doubled the path length of photons through the array. Over 80% of the incident light was absorbed in the NW array with a Ag back reflector, approaching the absorption measured by the array on the GaAs substrate (and including the contribution of the substrate to the overall absorption).

The optical absorption of these GaAs NW arrays is remarkable, given that the NWs comprised a 4% filling fraction and corresponded to only a 125 nm planar equivalent of GaAs, yet exhibited similar total optical absorption to that of a thick

planar GaAs film.<sup>27</sup> The results shown in Fig. 2 indicate that these arrays exhibit both antireflective and enhanced optical absorption characteristics. To explain these results, a full-field electromagnetic simulation and analytical modal analysis was performed for NW arrays that had a similar diameter, pitch and length to the as-grown NW arrays (see ESI† for a more detailed description of methods). As reported previously,<sup>28,29</sup> the array absorption characteristics varied with the wire diameter and length, as well as with the pitch of the array. For example, increasing the diameter of the nanowires red-shifted the absorption peak at 760 nm (see ESI†).

Fig. 2c compares the simulated absorption of the free-standing GaAs NW arrays, of arrays on a back reflector, and of arrays on a GaAs substrate at normal incidence. The simulations showed similar trends to those observed experimentally (Fig. 2a). Potential sources for the minor deviations between experiment and simulation include an experimentally broader distribution of wire diameters due to processing variations, and

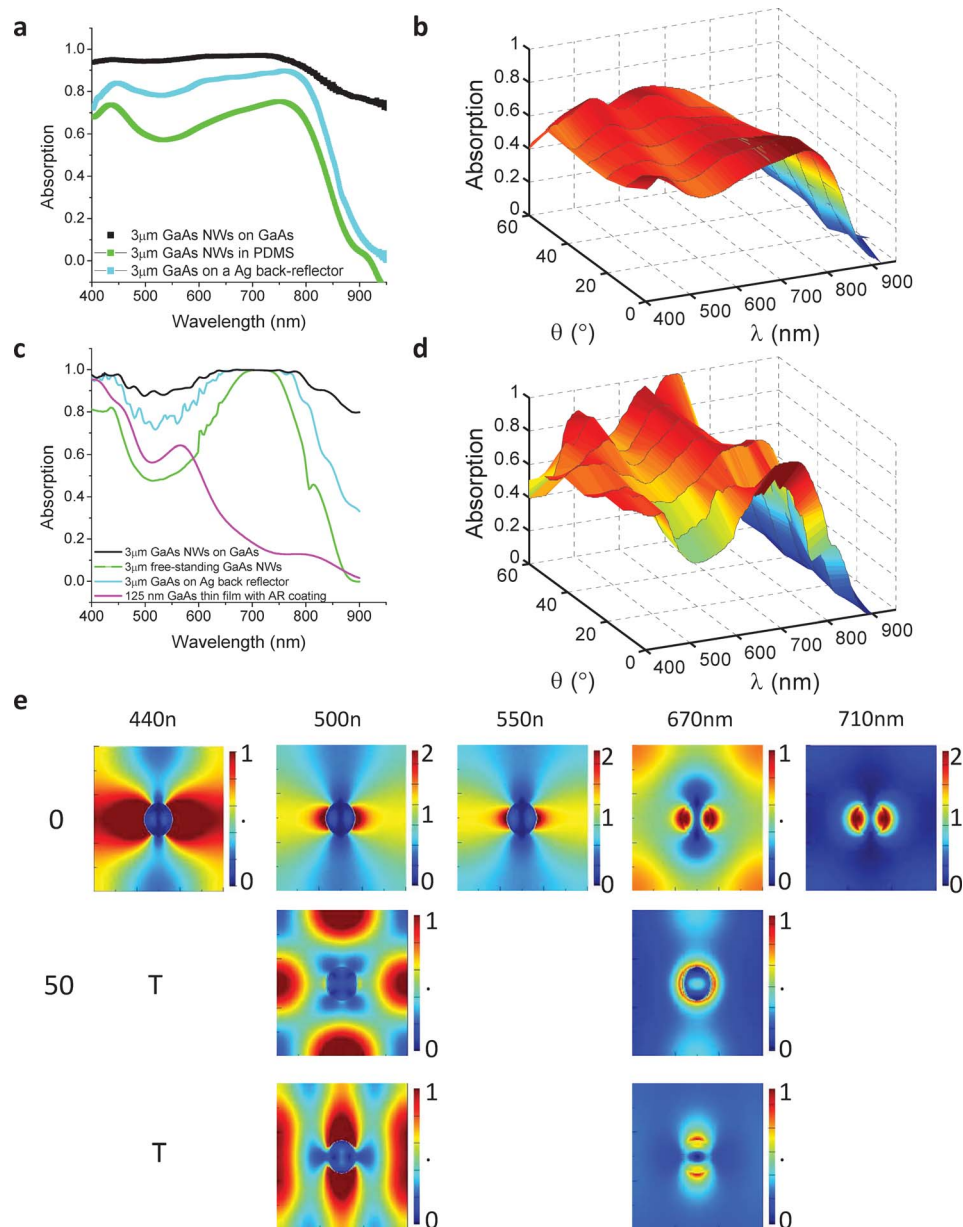


**Fig. 2** Experimental and simulated optical absorption of GaAs nanowire-arrays. (a) Overlaid normal-incidence absorption measurements of a GaAs NW array embedded in PDMS; a GaAs NW array embedded in PDMS on a Ag back-reflector; and an as-grown NW array on a GaAs substrate without a PDMS infill. (b) Angle-dependent optical absorption of a GaAs NW array embedded in a thin sheet of a peeled-off transparent PDMS film. (c and d) Simulation equivalents of a and b, and (e) simulated field intensity profiles at various wavelengths, incident angles and polarizations by 3D-FDTD methods, illustrating coupling into optical waveguide modes (field of view is one periodic unit of the NW array).

slightly off-normal growth due to a substrate miscut. Typically, these departures from perfect fidelity result in peak broadening and reduced absorption, which would account for the main discrepancy between the experiments and simulations. Similarly, Fig. 2b and d compare the experiment and simulation, respectively, of the wavelength- and angle-dependence of the absorption in peeled-off NW arrays. Again, the trends observed in the optical simulation agreed well with the experimental data.

A non-aqueous photoelectrochemical (PEC) method was employed to investigate the electrical and energy-conversion properties of GaAs NW arrays. A semiconductor/liquid junction

was formed between the as-grown n-GaAs NWs and the ferrocenium/ferrocene redox couple ( $\text{FcP}_2^{+/0}$ ) in dry acetonitrile ( $\text{CH}_3\text{CN}$ ) that contained lithium perchlorate as the supporting electrolyte. When n-GaAs NWs were brought into contact with this non-aqueous electrolyte, charge was transferred non-faradaically between the semiconducting photoelectrode and the electrolyte. Consequently, the photoelectrode had excess positive charge, due to the ionized dopants and spreading over the depletion width. A rectifying junction was therefore formed around each of the NWs, facilitating radial separation of photogenerated carriers. As shown in Fig. 3a, photogenerated holes (positively charged) inside the NW will diffuse and drift to the



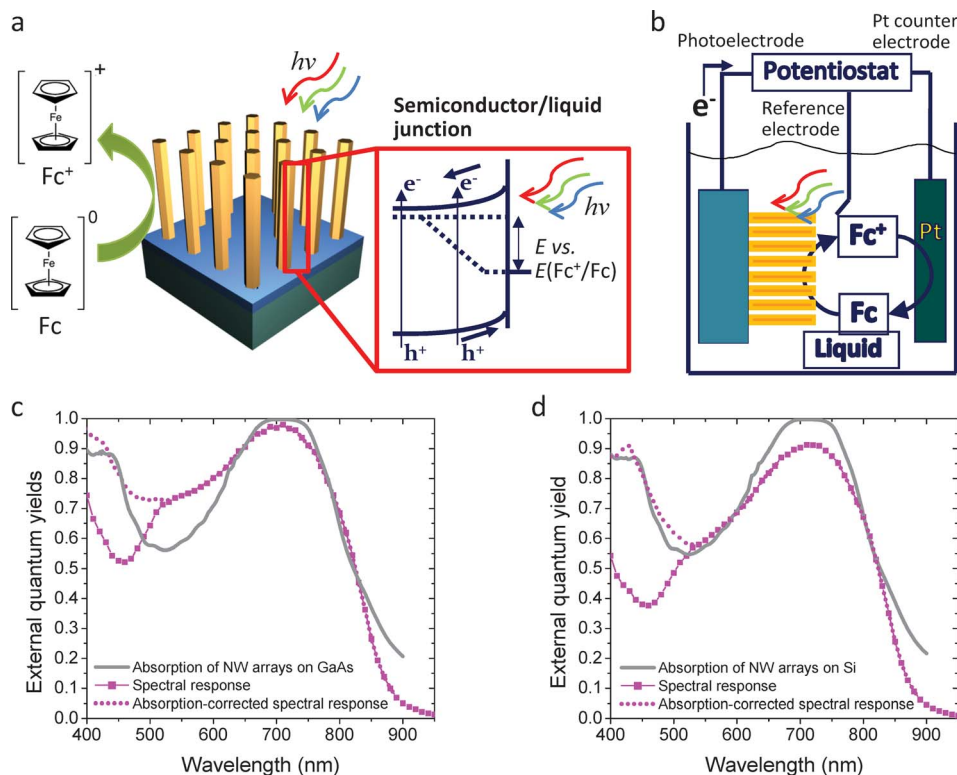


**Fig. 3** External quantum yields (EQYs) and simulated optical absorption of GaAs NW arrays, the experimental setup and principle of PEC measurements. (a) Schematics of a semiconductor/liquid junction and its energy band diagram under illumination. (b) Three-electrode potentiostatic setup of the non-aqueous PEC measurements. (c and d) Overlay of normal-incidence EQYs; of corrected EQYs taking into account absorption by the solution (see ESI†); and optical absorption of a GaAs NW array on GaAs (c) and on Si (d).

n-GaAs/liquid interface and oxidize the  $\text{FeCp}_2^0$  species to  $\text{FeCp}_2^+$ , contributing to the photocurrents. The conformal liquid contact therefore reveals the energy-conversion properties of the as-grown, three-dimensional GaAs NW arrays, by allowing measurement of current densities,  $J$ , at a given potential,  $E$ , of the Fermi level of the semiconductor relative to the electrochemical potential of solution that consists of a molecular redox pair formed from an oxidized species, A (e.g. ferrocenium), and a reduced species, A<sup>−</sup> (e.g. ferrocene). As shown in Fig. 3b, the reference electrode was poised at the solution potential, and the Pt counter electrode regenerated the  $\text{FeCp}_2^0$  species by reducing  $\text{FeCp}_2^+$ . The kinetically facile, one-electron, reversible  $\text{FeCp}_2^{+/0}$  redox couple was chosen to ensure that the electron-transfer kinetics at the semiconductor/liquid interface were not rate-limiting,<sup>30–32</sup> so that only the energy-conversion properties of GaAs NWs were measured. The reported data are for wire-arrays with a donor concentration that was found to maximize the open-circuit voltage (see ESI, Fig. S2†). The doping concentration of the NWs was controlled by specifying the  $\text{Si}_2\text{H}_6$  flow rate during the NW growth step.

The enhanced optical absorption of GaAs NW arrays, in conjunction with radial carrier-collection, resulted in high external quantum yields (EQYs) when these GaAs NW arrays were used as energy-conversion devices. The EQYs ( $\Phi_{\text{ext}}$ ) vs. wavelength were measured from photocurrent densities at normal incidence while the GaAs NW photoelectrodes were held at the solution potential. Fig. 3c shows the EQYs of GaAs

NW arrays on the GaAs substrate in contact with  $\text{CH}_3\text{CN}$ -ferrocene<sup>+/0</sup> ( $\text{FeCp}_2^{+/0}$ ), as well as the EQYs corrected for solution absorption, and the simulated absorption in the GaAs NW arrays on a GaAs substrate. The procedure used to obtain the solution-corrected collection efficiency is discussed in the ESI.† Fig. 3d is analogous to Fig. 3c but depicts the data for GaAs NWs that were grown on a Si substrate. No photocurrent was observed at wavelengths beyond 860 nm, indicating that the contribution to the photocurrents from the Si substrate was negligible.

Near-unity carrier collection efficiencies, *i.e.*, internal quantum yields (IQYs), were observed for broad ranges of photon energies above the band gap of GaAs. Because the radial dimension ( $\sim 67.5$  nm) is comparable to the diffusion length measured in a passivated GaAs NW,<sup>33</sup> complete carrier collection is expected (IQY = 1). This expectation is supported by the observation of near-unity IQYs at 760 nm for GaAs NWs on both GaAs and Si substrates. The observed decrease in the measured EQYs (solid purple curves in Fig. 3c and d) at  $\sim 450$  nm was due to solution absorption, which was measured and used for correction of the EQYs (see ESI†). The simulated optical absorption in the NW arrays matched well with the experimentally measured EQYs, again suggesting a nearly complete collection of photogenerated carriers.

Fig. 4 compares the current density vs. potential ( $J$ - $E$ ) behavior under illumination of n-GaAs NW arrays grown on n<sup>+</sup>-GaAs substrates relative to the behavior of planar n-GaAs

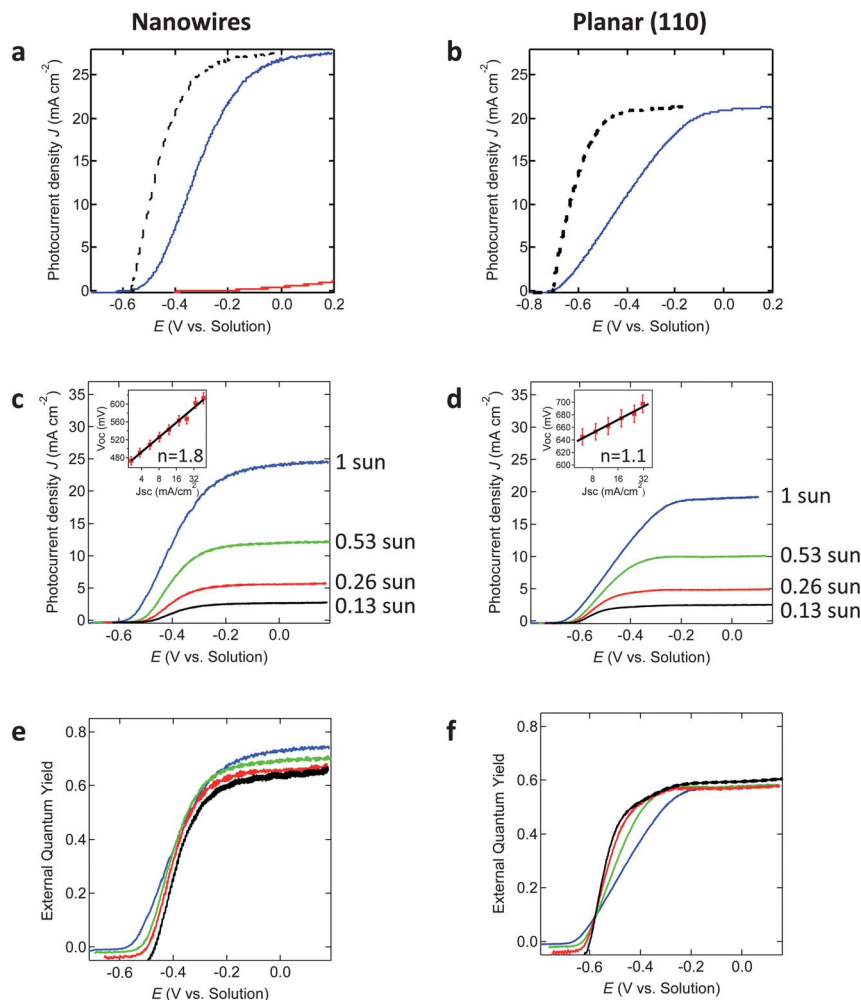


**Fig. 4** Photoelectrochemical current density-potential ( $J-E$ ) characteristics of n-GaAs NW/ $\text{CH}_3\text{CN-FeCp}_2^{+/0}$  and planar n-GaAs (110)/ $\text{CH}_3\text{CN-FeCp}_2^{+/0}$  junctions. (a and b) Overlay of  $J-E$  data for (a) GaAs NW arrays and (b) GaAs planar photoelectrodes, and the corresponding data corrected for the solution effects, including uncompensated electrochemical cell resistance ( $\sim 298$  ohms) and concentration overpotentials, so that the inherent properties of the photoelectrodes are displayed. The red curve in (a) shows the photoresponse of  $\text{n}^+\text{-GaAs (111)B}$  substrates with the nanowires physically removed. (c and d)  $J-E$  data of GaAs NW arrays and GaAs planar photoelectrodes as a function of the tungsten-halogen illumination intensity. In panel (e) and (f), the same data as in (c) and (d) are plotted in the form of integrated EQY, calculated based on the fraction of the measured photocurrent density relative to the estimated total photon flux at all energies above the band gap of GaAs.

photoanodes. Because the sidewalls of the NWs in the array (*i.e.* the junction area) were mainly comprised of {110} crystal facets, the  $J-E$  characteristics of planar n-GaAs {110} photoelectrodes were investigated for comparison to the behavior of the GaAs nanowires. The NW arrays (Fig. 4a, blue curve) produced an open-circuit voltage,  $V_{oc}$ , of  $590 \pm 15$  mV, a short-circuit current density,  $J_{sc}$ , of  $24.6 \pm 2.0$   $\text{mA cm}^{-2}$ , and a fill-factor, ff, of  $0.32 \pm 0.03$ , with an energy-conversion efficiency of 4.56% under tungsten-halogen ELH-type illumination that produced a current on a calibrated Si photodiode equivalent to that produced under  $100 \text{ mW cm}^{-2}$  AM1.5 G illumination. The  $\text{n}^+\text{-GaAs (111)B}$  substrates with the nanowires physically removed (Fig. 4a, red curve) produced a  $V_{oc}$  of  $202 \pm 3$  mV,  $J_{sc}$  of  $0.34 \pm 0.21$   $\text{mA cm}^{-2}$ , and ff of  $0.22 \pm 0.02$ . To ensure that the MOCVD growth step did not alter the substrate, electron-beam patterned  $\text{n}^+\text{-GaAs (111)B}$  substrates without growth of GaAs NWs were made into photoelectrodes and were found to

produce similar  $J-E$  characteristics to substrates from which the wires had been removed after growth. Due to the low photocurrent and poor diode characteristics of the substrate, the photoresponse of the NW arrays on the substrate was therefore almost completely associated with the NWs. After correcting for the concentration overpotential and uncompensated solution resistance losses (see ESI†), to thereby determine the intrinsic  $J-E$  behavior of the semiconductor photoelectrodes, the ff of n-GaAs NW arrays was determined to be  $0.56 \pm 0.02$ ,  $V_{oc}$  was  $590 \pm 15$  mV, and  $J_{sc}$  was  $24.6 \pm 2.0$   $\text{mA cm}^{-2}$ , resulting in a corrected efficiency ( $\eta_{eff}$ ) of 8.1%. The  $J_{sc}$  value is in good agreement with the integrated value for the AM 1.5G solar spectrum at 1-Sun obtained from the measured wavelength dependence of the EQY.

The planar n-GaAs photoelectrodes (Fig. 4b) displayed a  $V_{oc}$  of  $700 \pm 21$  mV,  $J_{sc}$  of  $20.1 \pm 2.3$   $\text{mA cm}^{-2}$ , and ff of  $0.31 \pm 0.03$ . Correcting for solution losses, the inherent photoelectrode

properties were  $ff = 0.66 \pm 0.04$ ,  $V_{oc} = 700 \pm 21$  mV,  $J_{sc} = 20.1 \pm 2.3$  mA cm<sup>-2</sup>, and  $\eta_{eff} = 9.2\%$ . The nanowire photoelectrodes exhibited a higher  $J_{sc}$  than the planar samples largely because the intrinsic antireflective nature of the NW arrays decreased the reflection losses in the NW-based system. In fact, the 700 mV  $V_{oc}$  from planar n-GaAs corresponds closely to the value obtained from bulk, defect-free, single-crystal GaAs (100) with an optimal n-type doping concentration in contact with this non-aqueous electrolyte.<sup>30</sup>

Fig. 4c and d show the effect of illumination intensity on the  $J$ - $E$  characteristics of n-GaAs NWs/CH<sub>3</sub>CN-FeCp<sub>2</sub><sup>+0</sup> and planar n-GaAs/CH<sub>3</sub>CN-FeCp<sub>2</sub><sup>+0</sup> junctions. The illumination from the ELH-type W-halogen lamp was attenuated through a series of neutral density filters, corresponding to 0.086–1.45 Sun, and the light-dependent  $V_{oc}$  vs.  $J_{sc}$  pairs were measured and are plotted in the insets of Fig. 4c and d. These data allowed for the determination of diode quality factor,  $n$ , via the following equation:<sup>34,35</sup>

$$V_{oc} = \frac{nkT}{q} \ln \left( \frac{J_{ph}}{\gamma J_0} + 1 \right) \quad (1)$$

where  $k$  is Boltzmann's constant,  $T$  is the absolute temperature,  $q$  is the unsigned charge on an electron,  $J_{ph}$  is the photocurrent density,  $J_0$  is the total recombination current density, and  $\gamma$  is the junction roughness factor which is the ratio of the junction area, or total surface area of NW arrays, to the geometric area of the NW photoelectrodes. The planar GaAs photoelectrodes exhibited a change in photovoltage of 52.5 mV as  $J_{sc}$  was varied from 6.1 to 31.3 mA cm<sup>-2</sup>, while the GaAs NW photoelectrodes exhibited a photovoltage change of 129.3 mV as the short-circuit current density changed from 2.3 to 30.8 mA cm<sup>-2</sup>. The diode quality factor was found to be 1.1 for planar n-GaAs/CH<sub>3</sub>CN-FeCp<sub>2</sub><sup>+0</sup> junctions, whereas  $n$  was 1.8 for n-GaAs NWs/CH<sub>3</sub>CN-FeCp<sub>2</sub><sup>+0</sup> contacts. Depletion-region recombination is significant for nanowires because the depletion regions make up the majority of the NW volume, which extends approximately 35 nm inward from the sidewall surfaces of the GaAs NWs.

Fig. 4e and f compare the potential dependence of the integrated EQYs for GaAs NW arrays and planar GaAs electrodes,

respectively, for the same illumination intensities shown in Fig. 4c and d. The integrated EQY was calculated by dividing the measured photocurrent density by the estimated total photon flux at all energies above the band gap of GaAs. As expected, the integrated EQYs measured at short circuit under various illumination intensities were constant, within experimental error. In contrast, the fill factors increased with decreasing photocurrent densities, indicating a significant solution resistance at a current density of >20 mA cm<sup>-2</sup> under 1-Sun illumination, thus justifying correction of the  $J$ - $E$  characteristics.

Mott-Schottky plots for n-GaAs NWs/CH<sub>3</sub>CN-FeCp<sub>2</sub><sup>+0</sup> and planar n-GaAs/CH<sub>3</sub>CN-FeCp<sub>2</sub><sup>+0</sup> electrodes were obtained by electrochemical impedance spectroscopy (Fig. 5a and b, and ESI†). The built-in voltage of n-GaAs (110)/CH<sub>3</sub>CN-FeCp<sub>2</sub><sup>+0</sup> junctions was determined to be  $1.23 \pm 0.04$  V from determination of the intercept of the inverse square of the differential capacitance ( $C_{diff}^{-2}$ ) as a function of the applied potential (Fig. 5b). The doping concentration of n-GaAs (110) (calculated from the Mott-Schottky plot) was  $3.11$ – $3.32 \times 10^{17}$ , in good agreement with the manufacturer's specification. By fitting the averaged slope in Fig. 5a with the numerical calculation (see ESI†), the doping concentration of the n-GaAs NWs was found to be  $2.45$ – $4.35 \times 10^{18}$  cm<sup>-3</sup>. The energetics of n-GaAs NWs/CH<sub>3</sub>CN-FeCp<sub>2</sub><sup>+0</sup> junctions were also estimated from the intercept with the horizontal axis, and yielded a built-in voltage of  $1.13 \pm 0.05$  V. The values for the built-in voltage fall within the range of values (1.05–1.27 V) reported previously for n-GaAs/liquid junctions in contact with the FeCp<sub>2</sub><sup>+0</sup> redox couple.<sup>31,32</sup>

The  $V_{oc}$  of the GaAs NWs/liquid junctions approached the recombination limit of bulk, defect-free, single-crystal GaAs, with a major voltage loss due to the five-fold increase in the junction area of the NW array relative to a planar sample. The experimentally observed  $V_{oc}$  from the NW array is determined by the separation of the electron and hole quasi-Fermi levels, which can also be estimated by the  $V_{oc}$  of the planar ( $V_{oc,planar}$ ) sample after correction for a series of voltage losses:

$$V_{oc,nanowires} \approx V_{oc,planar} - \frac{nkT}{q} \ln(\gamma) - V_{SRH} \quad (2)$$

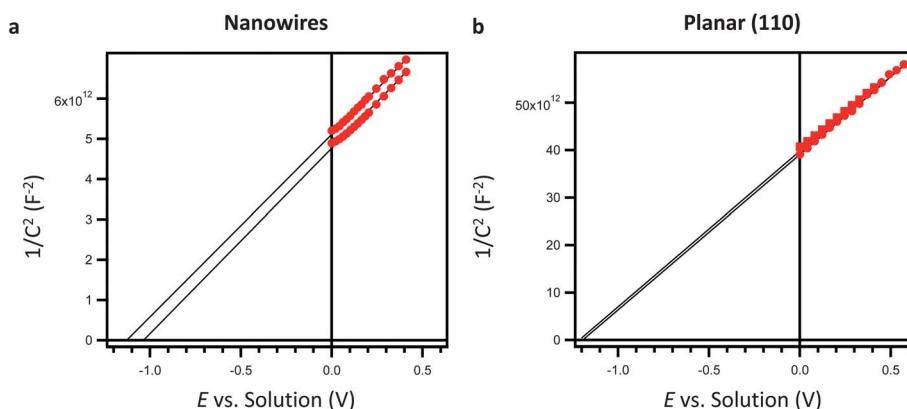


**Fig. 5** Mott-Schottky plots of (a) GaAs NW/CH<sub>3</sub>CN-FeCp<sub>2</sub><sup>+0</sup> and (b) planar GaAs (110)/CH<sub>3</sub>CN-FeCp<sub>2</sub><sup>+0</sup> junctions. The cell solution and configuration were the same as that used for the data of Fig. 3 and Fig. 4, and the measurements displayed in Fig. 5 were performed in the dark. The electrode areas were  $\sim 0.01$  cm<sup>2</sup> and  $\sim 0.3$  cm<sup>2</sup> for the nanowire and planar (110) photoelectrodes, respectively. The data represent upper bounds and lower bounds, respectively, on the measured built-in voltages.

where  $\frac{nkT}{q} \ln(\gamma)$  accounts for the loss due to photocurrents diluted over an increased junction area with a roughness factor  $\gamma$ , and  $V_{\text{SRH}}$  is defined as additional voltage loss in the nanowires, likely due to Shockley-Read-Hall recombination. The  $V_{\text{oc}}$  displayed by both planar (110)- and planar (100)-oriented n-GaAs is  $\sim 700$  mV in contact with the  $\text{FeCp}_2^{+/0}$  electrolyte. For the n-GaAs NW arrays,  $\gamma \approx 5$  and the diode quality factor equals 1.8, which corresponds to a voltage loss of  $\sim 75$  mV. Therefore, the 100 mV decrease in  $V_{\text{oc}}$  for the GaAs NW-array as compared to planar GaAs photoelectrodes arose primarily from the voltage loss due to an increase in the junction area in conjunction with the change in the diode quality factor. The remaining difference in  $V_{\text{oc}}$  might be due to (1) Shockley-Read-Hall recombination due to the presence of high density of twin defects in the nanowires (Fig. 1d) and/or (2) the distinctive behaviours of optical absorption and radiative emission in NW arrays.<sup>36</sup> Synthesis of twin-free III-V nanowires with either pure zinc-blende<sup>37,38</sup> or a pure Wurtzite structure<sup>39,40</sup> has been demonstrated by two-temperature VLS growth.<sup>41</sup> Nonetheless, the  $V_{\text{oc}}$  loss due to the roughness factor for defect-free NWs can be 46 mV at minimum ( $n = 1$ ), with an improvement of  $\sim 30$  mV possible. Furthermore, increasing the built-in voltage close to 1.42 V for GaAs, *e.g.* by forming a  $p^+-n$  junction or semiconductor/liquid junctions with more positive redox couple potentials, could increase the open-circuit photo-voltage by up to  $\sim 300$  mV.

In comparison to bulk or planar thin films of GaAs, the GaAs NW arrays exhibited dramatically enhanced optical absorption across the UV and visible portions of the solar spectrum, *via* scattering events and light trapping effects that minimized reflection losses. Because the dimensions of the GaAs NW arrays were on the order of the optical wavelength of light, a full wave-optics model analysis and simulation approach was performed to evaluate the observed optical behavior.<sup>42,43</sup> The anti-reflective characteristics of NW arrays with sub-wavelength features can be partially explained by the low filling fraction of NWs (only a few %), thereby reducing the fraction of reflected light.<sup>44</sup> In addition, when the wavelength of incident light is shorter than the dimensions of the GaAs NWs, multiple reflection and scattering events at the NW sidewalls and growth substrates may contribute to the enhanced absorption.<sup>45</sup>

A more comprehensive understanding of the absorption characteristics of the GaAs NW arrays, particularly those with diameters on the order of the wavelength of the incident light, requires examination of the spatially and spectrally dependent optical mode profiles (Fig. 2e). Light could conceivably couple into (i) guided and leaky optical waveguide modes (radial modes),<sup>29</sup> (ii) photonic crystal modes<sup>46</sup> or (iii) longitudinal modes (Fabry-Perot resonances) of NWs or NW arrays, resulting in enhanced absorption. The experimental and theoretical analysis of the absorption properties of these GaAs NW arrays suggested that guided and leaky optical waveguide modes were predominantly responsible for the high optical absorption and minimal reflection of the GaAs NW arrays at broadband wavelengths of 400–900 nm.

To further understand the observed enhancement in optical absorption, various optical simulations were used to identify the responsible optical modes. For the wire lengths used

experimentally, only very high-order longitudinal modes can be excited within the relevant spectral range of 400–900 nm, because only greater than 20<sup>th</sup> order modes exist for wire lengths  $L \approx 3 \mu\text{m}$ . Hence, absorption *via* longitudinal modes can be ruled out as the predominant contribution to the observed absorption enhancement. Wave interactions are possible in which the square array of NWs acts as a two-dimensional photonic crystal, but photonic crystal modes depend on both the radius of the wire and on the pitch of wires in the array, whereas the resonant wavelengths for optical waveguide modes in individual wires will depend only on the wire radius. Simulations for a range of wire radii and array pitches indicated that the spectral location of the strong absorption peaks depended only on the wire radius (see ESI<sup>†</sup>), suggesting that resonant optical waveguide modes are predominantly responsible for the observed enhanced absorption. Qualitatively similar profiles of the electric-field intensity were observed for an isolated individual wire and for a wire in the array, although the field magnitude of an isolated wire was much smaller (see ESI<sup>†</sup>) than that for wires in the array. These findings indicate that each wire acted as an independent optical waveguide. However, the “in-array” increase in modal intensity indicated that scattering off of neighboring wires enabled efficient incoupling into optical modes.

A detailed understanding of the absorption behavior required identification of the specific resonant optical waveguide modes that are responsible for each spectral peak. Such an in-depth understanding will facilitate optimization of the array dimensions to produce maximum light absorption. Electrical-field intensity of cross-sections of NW arrays was recorded at various incident angles and wavelengths for both TE and TM polarizations, and was compared with the calculated electric-field intensity profiles of the fundamental optical waveguide modes at their resonant wavelengths. Interestingly, the mode profiles calculated by conventional waveguide theory<sup>47,48</sup> can be directly compared to the observed electric-field intensity profiles of sub-wavelength NW cross-sections in FDTD simulations. Waveguide modes are typically denoted as  $\text{TM}_{mn}$  or  $\text{TE}_{mn}$ , where  $m$  and  $n$  are the azimuthal and radial mode numbers, respectively, indicating the number of field maxima in a given direction. The eigenvalue equations for both (1) confined and (2) leaky optical waveguide modes can be obtained (see ESI<sup>†</sup>) by solving Maxwell's equations under the constraint of continuity of the tangential  $z$ - and  $\theta$ -components of the electric and magnetic fields, yielding:

$$\left(\frac{1}{k_1^2} + \frac{1}{k_2^2}\right)^2 \left(\frac{\beta m}{k_0 a}\right)^2 = \left(\frac{n_1^2 J'_m(k_1 a)}{k_1 J_m(k_1 a)} + \frac{n_2^2 K'_m(k_2 a)}{k_2 K_m(k_2 a)}\right) \times \left(\frac{1 J'_m(k_1 a)}{k_1 J_m(k_1 a)} + \frac{1 K'_m(k_2 a)}{k_2 K_m(k_2 a)}\right) \quad (3)$$

$$\left(\frac{1}{k_1^2} - \frac{1}{k_2^2}\right)^2 \left(\frac{m}{k_0 a}\right)^2 = \left(\frac{n_1^2 J'_m(k_1 a)}{k_1 J_m(k_1 a)} - \frac{n_2^2 H'_m(k_2 a)}{k_2 H_m(k_2 a)}\right) \times \left(\frac{1 J'_m(k_1 a)}{k_1 J_m(k_1 a)} - \frac{1 H'_m(k_2 a)}{k_2 H_m(k_2 a)}\right) \quad (4)$$



where  $a$  is the wire radius,  $k_0$  and  $\beta$  are the total and z-component of the wave vector in free space,  $k_1$  ( $k_2$ ) and  $n_1$  ( $n_2$ ) are the transverse components of the wave vectors and refractive indices inside (outside) the nanowire, and  $J_m$ ,  $K_m$ , and  $H_m$  are the Bessel (1<sup>st</sup> kind), modified Bessel (2<sup>nd</sup> kind), and Hankel (1<sup>st</sup> kind) functions. Solutions to the eigenvalue equations for  $k_0$ , to obtain the resonant wavelengths for confined and leaky modes, occur at  $\beta = n_1 k_0$  and  $\beta = 0$ , respectively (Table 1; also see ESI† for the electric-field intensity profiles of each mode at their resonant wavelengths).

A comparison between the field profiles obtained *via* 3D FDTD simulation and these analytically calculated resonant wavelengths and electric-field intensity profiles provided a full explanation of the experimentally observed absorption trends. The following analysis examines and identifies the relevant modes at the normal incidence peaks (440 and 710 nm) and trough (550 nm) and at 50° incidence peaks (500 and 670 nm) for both TE and TM polarizations. The simulated electric field intensity profiles for these wavelengths are shown in Fig. 2e (at normal incidence, TE and TM polarizations are degenerate in a square-packed array of GaAs NWs).

At normal incidence (0° in Fig. 2e), the electric-field intensity profiles are confined to, and are more intense around, the wire at 440 and 710 nm (absorption peaks) than at 550 nm (absorption trough), revealing that the absorption peaks corresponded to coupling into resonant waveguide modes. The electric-field intensity profile at 710 nm has a dipole feature that is characteristic of the TM<sub>11</sub> mode, which matches precisely with the calculated wavelength of a leaky mode resonance. This peak was observed experimentally to be slightly red-shifted, to ~760 nm, corresponding to a wire radius of 72.5 nm. This value is within the distribution of wire radii in the array. As expected, this mode is also observable at 550 nm, but the incoupling efficiency is much lower than that at the resonant wavelength, as evidenced by the lower intensity profile of electric fields. At 440 nm, the mode profile within the wire is fainter because of

the large absorption coefficient of GaAs, and is characteristic of the leaky TM<sub>12</sub> mode profile, which is resonant at 400 nm. Thus, the two absorption peaks at normal incidence can be explained *via* an optical waveguide analysis.

In Fig. 2b and d, the angular-dependent absorption data revealed a shift in the resonant wavelengths at large incidence angles, indicating that light couples into additional optical modes. By comparing the intensity profiles of fundamental modes with the electric-field intensity profiles at the shifted peaks of 500 and 670 nm for 0° and 50° incidence (Fig. 2e), excitation of additional modes was confirmed at off-normal incidence. At 670 nm, the normal incidence field profile is nearly identical to that at 710 nm, which allows the characterization of the incoupling into the dipole TM<sub>11</sub> mode. At off-normal incidence, the TM-polarized field intensity has a center lobe feature that is highly concentrated in the NW, indicating that light is coupling into the guided TM<sub>01</sub> mode (calculated resonance at 650 nm). The TE polarized field exhibits an outer ring that is also fairly concentrated within the nanowire, characteristic of the TE<sub>01</sub> mode. At 500 nm, the TM-polarized wave exhibits a quadrupole feature in addition to the center lobe feature identified as the guided TM<sub>01</sub> mode at 670 nm. The quadrupole feature matches the leaky TM<sub>21</sub> mode, which matches extremely well with a calculated resonance at 500 nm. The TE-polarized wave exhibits an asymmetric inner intensity with an outer dipole character, which is characteristic of the leaky TE<sub>11</sub> mode (calculated resonance at 500 nm). Thus, all of the significant peaks in the angular and wavelength-dependent absorption spectrum of the GaAs NW-array can be explained by incoupling into resonant optical waveguide modes.

In conclusion, n-GaAs nanowire arrays were fabricated on GaAs and Si substrates using selective-area MOCVD growth. The optical absorption and spectral response data indicated near-unity internal quantum yields for photon energies above the band gap of GaAs, due to efficient incoupling into the resonant waveguide modes. In contact with a non-aqueous solvent, n-GaAs NW photoanodes produced inherent energy-conversion efficiencies of ~8.1%, with open-circuit photovoltages of 590 mV and short-circuit current densities of 24.6 mA cm<sup>-2</sup>. These results demonstrate that n-GaAs nanowire arrays are excellent light absorbers with the potential for high solar energy-conversion efficiency, providing a significant step towards dual-junction systems that integrate III-V nanowires and Si for scalable solar energy conversion and storage applications.

## Methods

### Selective-area growth of GaAs nanowires

Fig. 1e illustrates the process schematics that were used to perform selective-area growth by MOCVD. A thin layer of 30 nm thick SiN<sub>x</sub> was deposited onto the GaAs (111)B surface by plasma-enhanced chemical-vapor deposition (PECVD). Electron-beam lithography was then used to define square-arrays of 100 nm diameter holes on a 600 nm pitch. The square array was 1 mm by 1 mm in size, and was surrounded by a skirt region that consisted of an exposed GaAs surface. The skirt region was used to absorb excess gas-phase precursors, because a lack of

**Table 1** Calculated and observed resonant wavelengths for optical waveguide modes of GaAs NWs with a radius of 67.5 nm

$m^a$	Leaky				Guided	
	$n^b$					
	1	2	1			
TE	Calc.	Obs.	Calc.	Obs.	Calc.	Obs.
0	770	— <sup>c</sup>	425	— <sup>c</sup>	650	670
1	500	500	<300	— <sup>c</sup>	∞	— <sup>c</sup>
2	430	— <sup>c</sup>	<300	— <sup>c</sup>	<300	— <sup>c</sup>
TM						
0	1770	— <sup>c</sup>	480	— <sup>c</sup>	650	670
1	710	710	400	440	480	— <sup>c</sup>
2	500	500	<300	— <sup>c</sup>	420	— <sup>c</sup>
3	420	— <sup>c</sup>	<300	— <sup>c</sup>	<300	— <sup>c</sup>

<sup>a</sup>  $m$ : azimuthal mode number. <sup>b</sup>  $n$ : radial mode number. <sup>c</sup> —: indicates that the mode was not observed in the simulated field profiles.

deposition of GaAs on the SiN<sub>x</sub> mask affected the growth behavior of GaAs in the square-array region.

Growth of GaAs NWs was performed on the nanopatterned samples using a vertical, showerhead, low-pressure MOCVD reactor that was operated at 0.1 atm. Trimethylgallium (TMGa) was the precursor for the group III element, arsine (As<sub>2</sub>H<sub>6</sub>) was the precursor for the group V element, and disilane was the n-dopant precursor. GaAs NWs were grown in a H<sub>2</sub>(g) atmosphere with a V/III ratio of 127, at a partial pressure of  $3.74 \times 10^{-7}$  atm for TMGa and of  $4.78 \times 10^{-5}$  atm for arsine. The growth rate of the NWs was  $\sim 8.33 \text{ \AA s}^{-1}$ , as calibrated from a 30 min growth at 790 °C.

### Exfoliation of polymer-infilled GaAs nanowire-arrays

GaAs NW arrays were infiltrated with a polymer using a procedure that closely followed a published method.<sup>49</sup> After infiltration, the arrays were peeled-off from the underlying wafer. The polydimethylsiloxane (PDMS) base and curing agent were mixed in a 10 : 2 w/w ratio and then sonicated (Sylgard 184, Dow Corning). This mixture was spin-coated for 1 min at 1000 rpm onto the wire arrays, degassed for 30 min, and then cured overnight at 80 °C. The polymer-infilled GaAs NW arrays were mechanically removed from the underlying GaAs substrate by use of tweezers.

### Optical absorption and reflection measurements

Wavelength-dependent absorption spectra and reflection measurements were obtained using a UV-vis spectrometer (Varian Cary 5000) that was equipped with an integrating sphere. A small-spot kit was used to produce a beam size of <1 mm (FWHM) for focused illumination. The divergence angle of the incident beam was 9°. The internal surfaces of the sphere, baffles, port blocks and port apertures were coated with a barium sulfate coating, to achieve nearly ideal Lambertian reflectivity. In a center-mount mode for absorption measurements of non-opaque samples (e.g. GaAs NW arrays embedded in peeled-off PDMS), each sample was supported on a quartz slide that was placed at the center of the sphere. In a rear-mount mode for reflection measurements of opaque samples (e.g. as-grown GaAs NW arrays on GaAs or Si substrates, GaAs NW arrays embedded in PDMS placed on a Ag back reflector), each sample was mounted behind a 2 mm diameter port aperture at the rear port of the sphere, with light at normal incidence. More detailed procedures for the determination of the absorption of the samples are described in the ESI.†

### Electrode fabrication

1 mm by 1 mm arrays of GaAs nanowires were grown in the center of 5 mm by 5 mm square pieces of n<sup>+</sup>-GaAs substrates. Sequential evaporation of metal films on the backside of the chip was used to provide the electrical contacts, which consisted of a layered stack of 100 nm Au–Ge eutectic alloy (12 wt% Ge)/30 nm nickel/100 nm gold, followed by rapid thermal annealing in forming gas (4% H<sub>2</sub> in N<sub>2</sub>) at 400 °C for 1 min. The chip was then attached to a coiled, tin-plated Cu wire using conductive Ag paint, and epoxy (Hysol 9460F) was used to seal, face-down, the assembly at the end of a segment of glass tubing. The active area of each electrode was defined by the epoxy, with a typical

value of 0.009 cm<sup>2</sup>. Only the GaAs nanowire array was exposed to the electrolyte, while the remaining area of the chip was covered by sputtered SiN<sub>x</sub> and then by epoxy.

Prior to photoelectrochemical measurements, the n-GaAs nanowire-array and planar n-GaAs photoelectrodes were etched in a solution of 0.04% (v/v) Br<sub>2</sub> in methanol (CH<sub>3</sub>OH, low water, J. T. Baker) for 15 s, followed by immersion in 1.0 M KOH(aq) for 15 s. The KOH solution was then replaced with 2.0 M NH<sub>3</sub> in CH<sub>3</sub>OH, after which the electrode was dried in a flow of N<sub>2</sub>(g) and quickly transferred into a glovebox that was continually purged with ultra-high purity (UHP) argon.

### Photoelectrochemical (PEC) measurements

For the non-aqueous PEC experiments, acetonitrile (CH<sub>3</sub>CN, anhydrous, 99.8%, Sigma Aldrich) was dried by flowing through a solvent column and storing the solvent over 3 Å activated molecular sieves. LiClO<sub>4</sub> (battery grade, 99.99%, Sigma Aldrich) was dried by fusing the salt under  $<1 \times 10^{-3}$  Torr at 300 °C, and the resulting material was stored under UHP Ar(g) that contained <0.2 ppm O<sub>2</sub>(g). Bis(cyclopentadienyl) iron(II) (ferrocene, FeCp<sub>2</sub><sup>0</sup>) was purchased from Sigma Aldrich and was purified by sublimation *in vacuo*. Bis(cyclopentadienyl) iron(III) tetrafluoroborate (ferrocenium, FeCp<sub>2</sub><sup>+</sup>·BF<sub>4</sub><sup>−</sup>) was purchased from Sigma Aldrich, recrystallized in a mixture of diethyl ether and acetonitrile, and dried *in vacuo* before use.

A standard three-electrode potentiostatic setup, with ferrocenium/ferrocene (FeCp<sub>2</sub><sup>+</sup>/FeCp<sub>2</sub><sup>0</sup>) as the redox couple and dry acetonitrile (CH<sub>3</sub>CN) as the solvent, was used for all of the photoelectrochemical experiments. The reference electrode was a Pt wire poised at the solution potential, and the counter electrode was a Pt mesh with an area more than 10 times larger than the working electrode. The working photoelectrodes were oriented vertically downward and were illuminated by an ELH-type tungsten–halogen bulb whose intensity was adjusted by the use of neutral density filters. To obtain the photoelectrochemical data, all three electrodes were immersed in a dry CH<sub>3</sub>CN solution that contained 0.5 mM ferrocenium, 90 mM ferrocene, and 1.0 M LiClO<sub>4</sub> as the supporting electrolyte. The solution was vigorously stirred to minimize mass-transport limited effects on the current density. Current density vs. potential (*J*–*E*) data were collected at 50 mV s<sup>−1</sup> using a Gamry Reference 600 potentiostat. External quantum yield and Mott–Schottky measurements used the same electrochemical setup as that used for the collection of the *J*–*E* data.

### Simulation setup for optical absorption

The Lumerical FDTD Solutions Software Package was used for 3D full-field electromagnetic simulations of the GaAs NWs. The standard wire dimensions were  $L = 3.24 \text{ \mu m}$ ,  $R = 67.5 \text{ nm}$ , and pitch = 600 nm. For the wires on Si substrates, a value of  $L = 2.5 \text{ \mu m}$  was used. The NW arrays were modeled using periodic boundary conditions at normal incidence and Bloch boundary conditions at off-normal angles. Broadband simulations were used with a range of 350–900 nm, and the absorption was calculated from transmission and reflection monitors in 2 nm intervals. At normal incidence, the TE and

TM polarizations are degenerate, so the behavior of only one polarization was computed. At off-normal incidence, both polarizations were simulated and the results were averaged to produce a result for the total absorption, to thereby simulate the situation in unpolarized sunlight. For normal incidence, profiles of the electric field intensity were obtained by recording the electric field data with a 3-D field profile monitor in 10 nm wavelength intervals. At off-normal incidence, single-wavelength simulations were used to record the electric field data, due to angular distributions that are intrinsic to nonzero angles of illumination for broad-band simulations in Lumerical FDTD.

## Acknowledgements

The non-aqueous photoelectrochemistry and optical simulation was supported by the Office of Science of the U.S. Department of Energy under Award no. DE-SC0004993 to the Joint Center for Artificial Photosynthesis, a DOE Energy Innovation Hub; and the MOCVD growth was supported by the Center for Energy Nanoscience, an Energy Frontier Research Center funded by the U.S. Department of Energy, Office of Basic Energy Sciences under Award Number DE-SC0001013. The authors acknowledge Professor Hans-Joachim Lewerenz, Professor Michelle Povinelli and Stanley Burgos for helpful discussions, and Dr Ron Grimm for assistance with the photoelectrochemical studies. Optical data were collected at the Molecular Materials Research Center of the Beckman Institute of the California Institute of Technology. M.Y. acknowledges a USC Provost's Ph.D. Fellowship and K. T. F. acknowledges the National Science Foundation for Graduate Research Fellowship under Grant no. DGE-1144469.

## Notes and references

- 1 M. G. Walter, E. L. Warren, J. R. McKone, S. W. Boettcher, Q. Mi, E. A. Santori and N. S. Lewis, *Chem. Rev.*, 2010, **110**, 6446–6473.
- 2 C. H. Henry, *J. Appl. Phys.*, 1980, **51**, 4494.
- 3 T. Takamoto, T. Agui, E. Ikeda and H. Kurita, *Sol. Energy Mater. Sol. Cells*, 2001, **66**, 511–516.
- 4 H. Kroemer, T.-Y. Liu and P. M. Petroff, *J. Cryst. Growth*, 1989, **95**, 96–102.
- 5 Y. Shimizu and Y. Okada, *J. Cryst. Growth*, 2004, **265**, 99–106.
- 6 E. Ertekin, P. A. Greaney, D. C. Chrzan and T. D. Sands, *J. Appl. Phys.*, 2005, **97**, 114325.
- 7 L. C. Chuang, M. Moewe, C. Chase, N. P. Kobayashi, C. Chang-Hasnain and S. Crankshaw, *Appl. Phys. Lett.*, 2007, **90**, 043115.
- 8 M. Bosi and C. Pelosi, *Progress in Photovoltaics: Research and Applications*, 2007, **15**, 51–68.
- 9 J. F. Geisz and D. J. Friedman, *Semicond. Sci. Technol.*, 2002, **17**, 769–777.
- 10 R. R. King, D. C. Law, K. M. Edmondson, C. M. Fetzer, G. S. Kinsey, H. Yoon, R. A. Sherif and N. H. Karam, *Appl. Phys. Lett.*, 2007, **90**, 183516.
- 11 J. F. Geisz, D. J. Friedman, J. S. Ward, A. Duda, W. J. Olavarria, T. E. Moriarty, J. T. Kiehl, M. J. Romero, A. G. Norman and K. M. Jones, *Appl. Phys. Lett.*, 2008, **93**, 123505.
- 12 T. J. Kempa, J. F. Cahoon, S.-K. Kim, R. W. Day, D. C. Bell, H.-G. Park and C. M. Lieber, *Proc. Natl. Acad. Sci. U. S. A.*, 2012, **109**, 1407–1412.
- 13 G. Mariani, P.-S. Wong, A. M. Katzenmeyer, F. Léonard, J. Shapiro and D. L. Huffaker, *Nano Lett.*, 2011, **11**, 2490–2494.
- 14 S. R. Kurtz, P. Faine and J. M. Olson, *J. Appl. Phys.*, 1990, **68**, 1890.
- 15 M. D. Archer and J. R. Bolton, *J. Phys. Chem.*, 1990, **94**, 8028–8036.
- 16 M. Umeno, T. Soga, K. Baskar and T. Jimbo, *Sol. Energy Mater. Sol. Cells*, 1998, **50**, 203–212.
- 17 I. Vurgaftman, J. R. Meyer and L. R. Ram-Mohan, *J. Appl. Phys.*, 2001, **89**, 5815.
- 18 C. P. T. Svensson, T. Mårtensson, J. Trägårdh, C. Larsson, M. Rask, D. Hessman, L. Samuelson and J. Ohlsson, *Nanotechnology*, 2008, **19**, 305201.
- 19 F. Jabeen, G. Patriarche, F. Glas and J.-C. Harmand, *J. Cryst. Growth*, 2011, **323**, 293–296.
- 20 J. Noborisaka, J. Motohisa and T. Fukui, *Appl. Phys. Lett.*, 2005, **86**, 213102.
- 21 H.-J. Chu, T.-W. Yeh, L. Stewart and P. D. Dapkus, *Phys. Status Solidi C*, 2010, **7**, 2494–2497.
- 22 K. Tomioka, P. Mohan, J. Noborisaka, S. Hara, J. Motohisa and T. Fukui, *J. Cryst. Growth*, 2007, **298**, 644–647.
- 23 B. Hua, J. Motohisa, Y. Kobayashi, S. Hara and T. Fukui, *Nano Lett.*, 2009, **9**, 112–116.
- 24 K. Tomioka, J. Motohisa, S. Hara and T. Fukui, *Nano Lett.*, 2008, **8**, 3475–3480.
- 25 T. Mårtensson, C. P. T. Svensson, B. A. Wacaser, M. W. Larsson, W. Seifert, K. Deppert, A. Gustafsson, L. R. Wallenberg and L. Samuelson, *Nano Lett.*, 2004, **4**, 1987–1990.
- 26 M. Heurlin, P. Wickert, S. Fält, M. T. Borgström, K. Deppert, L. Samuelson and M. H. Magnusson, *Nano Lett.*, 2011, **11**, 2028–2031.
- 27 N. Huang, C. Lin and M. L. Povinelli, *J. Appl. Phys.*, 2012, **112**, 064321.
- 28 J. Kupec and B. Witzigmann, *Opt. Express*, 2009, **17**, 10399–10410.
- 29 L. Cao, J. S. White, J.-S. Park, J. A. Schuller, B. M. Clemens and M. L. Brongersma, *Nat. Mater.*, 2009, **8**, 643–647.
- 30 C. M. Gronet and N. S. Lewis, *Appl. Phys. Lett.*, 1983, **43**, 115–117.
- 31 L. G. Casagrande, A. Juang and N. S. Lewis, *J. Phys. Chem. B*, 2000, **104**, 5436–5447.
- 32 B. Ba, H. Cachet, B. Fotouhi and O. Gorochov, *Semicond. Sci. Technol.*, 1994, **9**, 1529–1534.
- 33 C.-C. Chang, C.-Y. Chi, M. Yao, N. Huang, C.-C. Chen, J. Theiss, A. W. Bushmaker, S. Lalumondiere, T.-W. Yeh, M. L. Povinelli, C. Zhou, P. D. Dapkus and S. B. Cronin, *Nano Lett.*, 2012, **12**, 4484–4489.
- 34 K. E. Pomykal, A. M. Fajardo and N. S. Lewis, *J. Phys. Chem.*, 1996, **100**, 3652–3664.

- 35 S. W. Boettcher, J. M. Spurgeon, M. C. Putnam, E. L. Warren, D. B. Turner-Evans, M. D. Kelzenberg, J. R. Maiolo, H. A. Atwater and N. S. Lewis, *Science*, 2010, **327**, 185–187.
- 36 J. Kupec and R. Stoop, *Opt. Express*, 2010, **18**, 4651–4656.
- 37 P. Caroff, K. A. Dick, J. Johansson, M. E. Messing, K. Deppert and L. Samuelson, *Nat. Nanotechnol.*, 2009, **4**, 50–55.
- 38 K. A. Dick, P. Caroff, J. Bolinsson, M. E. Messing, J. Johansson, K. Deppert, L. R. Wallenberg and L. Samuelson, *Semicond. Sci. Technol.*, 2010, **25**, 024009.
- 39 H. J. Joyce, J. Wong-Leung, Q. Gao, H. H. Tan and C. Jagadish, *Nano Lett.*, 2010, **10**, 908–915.
- 40 K. Ikejiri, Y. Kitauchi, K. Tomioka, J. Motohisa and T. Fukui, *Nano Lett.*, 2011, **11**, 4314–4318.
- 41 H. J. Joyce, Q. Gao, H. H. Tan, C. Jagadish, Y. Kim, X. Zhang, Y. Guo and J. Zou, *Nano Lett.*, 2007, **7**, 921–926.
- 42 N. Huang, C. Lin and M. L. Povinelli, *J. Opt.*, 2012, **14**, 024004.
- 43 A. R. Madaria, M. Yao, C. Chi, N. Huang, C. Lin, R. Li, M. L. Povinelli, P. D. Dapkus and C. Zhou, *Nano Lett.*, 2012, **12**, 2839–2845.
- 44 D. L. Brundrett, E. N. Glytsis and T. K. Gaylord, *Appl. Opt.*, 1994, **33**, 2695–2706.
- 45 M. D. Kelzenberg, S. W. Boettcher, J. A. Petykiewicz, D. B. Turner-Evans, M. C. Putnam, E. L. Warren, J. M. Spurgeon, R. M. Briggs, N. S. Lewis and H. A. Atwater, *Nat. Mater.*, 2010, **9**, 239–244.
- 46 C. Lin and M. L. Povinelli, *Opt. Express*, 2009, **17**, 19371–19381.
- 47 J. A. Kong, *Electromagnetic Wave Theory*, Wiley, 1990.
- 48 R. Black and L. Gagnon, *Optical Waveguide Modes: Polarization, Coupling and Symmetry*, McGraw-Hill, 2010.
- 49 J. M. Spurgeon, S. W. Boettcher, M. D. Kelzenberg, B. S. Brunschwig, H. A. Atwater and N. S. Lewis, *Adv. Mater.*, 2010, **22**, 3277–3281.